Rethinking transport
27–30 April 2020

TRA 2020 TRANSPORT RESEARCH ARENA HELSINKI

Proceedings of 8th Transport Research Arena TRA 2020, April 27-30, 2020, Helsinki, Finland

Induction motor design tool for drivetrain applications

Lauriane Prongué[a]*, Nicolas Broch[a], Tobias Wellerdieck[a]

[a]*BRUSA Elektronik AG, Neudorf 14, Sennwald 9466, Switzerland*

Abstract

In this paper, an analytical design tool for the development of induction motors in automotive traction drivetrain applications is presented. The software was developed by *BRUSA Elektronik AG* to accelerate motor design development. The main motivation for the introduction of the new tool originates from the decreasing product life cycles of electrified drivetrains compared to classical internal combustion engines. This trend is mainly driven by the switch towards hybrid and battery electric vehicles. The novel design tool optimizes the motor topology using analytical formulas considering automotive requirements, key performance indicators, and motor control strategy. The analytical approach allows for short computation times. This facilitates the analysis of a wide design space and the subsequent reduction to a manageable set of promising designs. The different parts of the design tool are described in detail in this paper and its accuracy is discussed with an example of a traction drive.

Keywords: induction motor; analytical motor design; efficiency optimization; automotive drivetrain; machine optimization.

* Corresponding author. Tel.: +4181-758-0997;
E-mail address: lauriane.prongue@brusa.biz

1. Introduction

BRUSA Elektronik AG is a leading provider of engineering solutions and products in the e-mobility sector. For 35 years, the company designs and manufactures small, light and efficient electrical and mechanical components for electric powertrains. *BRUSA* aims at developing sustainable technologies and products to preserve our environment and climate.

The e-mobility sector, being relatively new compared to combustion engines, still offers a vast improvement and expansion potential. Battery Electric Vehicles (BEVs) represent approximately 2 % of the global light vehicle market. The growth of the BEVs' market share is exponential, and it is estimated that by 2025 around 10 % of the global market sales will be BEVs, Raconteur (2018), J.P.Morgan (2018), McKinsey (2018).

The automotive industry is an exacting sector; each motor is designed to fulfill challenging requirements including efficiency, weight, volume, cost and power density. The motor topologies for drivetrain applications must be optimized to a higher standard than industrial general-purpose motors. Furthermore, the reduced life cycle of electrified drivetrains compared to internal combustion engines increases the relevance of fast design development. Currently, motor development relies heavily on the use of expensive proprietary Finite Element Method (FEM) software requiring significant computing power. Simulating a single load point of a machine design can take several minutes. Thus, FEM tools are inadequate to perform a first topology optimization and cover a large design space. To solve this problem and accelerate the development process, *BRUSA* developed an analytical design tool for induction motors.

The high computation speed of Lightning Analytical Motor Analysis (LAMA) tool is achieved by using analytical motor models complemented by empirical factors. The investigation of a motor topology, consisting of an efficiency map for the whole speed and torque range, is carried out in about one and a half minutes on a standard workstation. The same analysis using FEM simulations takes about 24 hours on said workstation making LAMA approximately 1000 times faster, c.f. Table 1. This allows the designer to cover a large design space and carry out a sensitivity analysis (of the most relevant parameters) or even an optimization.

Table 1. Computational speed comparison between the novel tool (LAMA) and state of the art FEM tools using a standard workstation.

Speed comparison	LAMA	FEM	Comment
Computation time for one topology	80 s	24 hours	Including efficiency map
Number of topologies optimized in a month	1000	5	Considering input/output overhead

A complete machine development is carried by first reducing the design space with the analytical tool and then refining the most promising designs using FEM. Therefore, the number of FEM simulations required is minimized, computation time is spared, and the development time is considerably reduced.

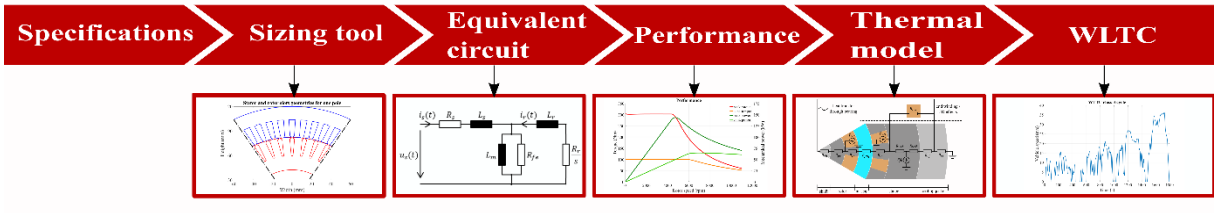

Fig. 1 LAMA computation workflow showing the three different motor models (geometrical, electrical and thermal lumped parameter) as well as performance results and WLTC estimation.

LAMA, as described in Fig. 1, consists of a sizing tool which minimizes the volume required to achieve a certain torque at a given speed (operating point), as derived in Boglietti et al. (2012). If the volume of the motor is fixed due to constraints from the vehicle integration, which is often the case, only the rotor diameter is optimized. Once the motor geometry is defined, the equivalent circuit parameters are computed as shown in Boglietti et al. (2011) and a no-load analysis as well as a locked rotor analysis are conducted. The T-equivalent circuit is used to determine the capability of the motor by driving it with open-loop voltage and frequency control. Based on these

results, the performance of the motor is evaluated with the use of a closed-loop control algorithm which minimizes the conductive losses. Afterwards, an efficiency map is generated, and the thermal behavior of the machine is analyzed. Finally, the motor performance is evaluated with a vehicle model driving the Worldwide harmonized Light vehicles Test Cycle (WLTC). An estimation of the driving range and WLTC efficiency of the given car facilitates the comparison of different traction motor designs. In section 2, the different parts of LAMA are discussed in detail. The accuracy of the tool is assessed in section 3 comparing LAMA results to measurements for a traction drivetrain motor. This induction motor is used as reference for all plots in this paper.

2. Analytical design tool for induction motors

The induction motor design tool consists of six different parts that can be used independently:

- Sizing tool
- Equivalent circuit tool
- Control strategy tool
- Thermal tool
- WLTC computation tool
- Cost computation tool

The sizing tool is comprised of an iterative process which optimizes the volume of the motor and computes its geometry. If the motor topology is already known, the sizing part is skipped, and the equivalent circuit tool is used to calculate the parameters of the motor. The equivalent circuit parameters are computed based on the motor geometry, its materials properties and the temperature of the motor. To account for temperature dependent material properties, an initial temperature is assumed. The exact operating point is then evaluated iteratively. The equivalent circuit parameters are input parameters to the control strategy tool which calculates the motor performance. A traction drivetrain motor performance consists of the torque versus speed curves in peak and continuous operation, as well as the efficiency map. The computed losses are then used in the thermal tool to calculate the temperature distribution in the motor. Usually two to three iterations of parameters, performance and temperature computations are required for the temperatures to converge. Finally, the efficiency map is used in the WLTC tool to evaluate the energy consumption of the drive system in a certain vehicle. This allows for an estimation of the driving range.

2.1. Sizing tool

The first part of LAMA is the sizing tool, c.f. Fig. 2. The user can specify an operating point, i.e. a given torque at a given speed, and the volume of the motor is optimized accordingly, Boglietti et al. (2012).

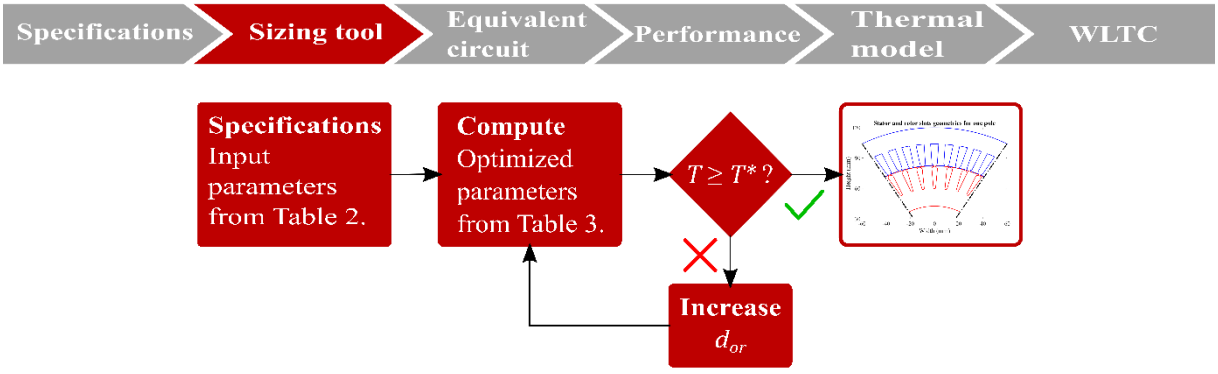

Fig. 2 The sizing tool defines the motor geometry based on performance requirements (torque, speed) and material properties.

First, a small rotor diameter is chosen, and the active length is calculated using the motor aspect ratio λ. Then, a fixed value of flux density is assumed in the air gap, and the stator and rotor teeth widths are determined using this value and the target flux densities in the teeth. This is described as

$$w_{ts/r} \propto \frac{B_{gp}\pi d_{or}}{Q_{s/r}B_{ts/r}}. \quad (1)$$

The fixed and optimized parameters used in the sizing tool are shown in Table 2 and Table 3, respectively. The magnetic flux of a pole is calculated using the fixed flux density in the air gap

$$\phi_{pole} \propto B_{gp} l_a \frac{\pi d_{or}}{N_{pp}}. \quad (2)$$

This flux is in turn used to calculate the stator and the rotor yoke widths considering their respective target flux densities

$$w_{ys/r} \propto \frac{\phi_{pole}}{B_{ys/r} l_a}. \quad (3)$$

Afterwards, the rotor current density is used to compute the peak current value, of the sinusoidal current distribution, flowing in the rotor bar I_{bar}. The torque, which is proportional to the current flowing in the rotor bars and the flux in the air gap is calculated according to

$$T \propto B_{gp} l_a d_{or} I_{bar} Q_r, \quad (4)$$

If the actual torque T is smaller than the target torque T^*, the rotor diameter is increased, and the operation is repeated. Otherwise, the stator outer diameter is calculated using the stator current density and the current flowing in the machine. The motor topology is now fully dimensioned, that is, the input parameters shown in Table 2 and the optimized parameters in Table 3 are defined.

Table 2. Fixed input parameters for the sizing tool.

Description	Variable	Comment	Description	Variable	Comment
Target torque	T^*	Target operating point	Ratio of active length to rotor diameter	λ	Aspect ratio of the motor
Target speed	n^*	Target operating point	Flux density in the air gap	B_{gp}	About 1 T (air capability)
DC-link voltage	U_{dc}	Usually battery voltage	Flux density in the stator/rotor teeth	$B_{ts/r}$	Below iron saturation, 1.7 T – 1.8 T
Number of pole pairs	N_{pp}	Increase to reduce yoke height	Flux density in the stator/rotor yoke	$B_{ys/r}$	Below iron saturation, 1.7 T – 1.8 T
Number of stator/rotor slots	$Q_{s/r}$	Chosen to reduce harmonics	Stator/rotor current density	$J_{s/r}$	Reduce to reduce temperature

Table 3. Parameters optimized by the sizing tool.

Description	Variable	Comment	Description	Variable	Comment
Stator/rotor outer diameter	$d_{os/r}$	Increase to increase the torque	Magnetic flux of a pole	ϕ_{pole}	Depends on B_{gp} and l_a
Active length	l_a	Increase to increase the torque	Rotor slot area	A_{sr}	Depends on w_{tr} and w_{yr}
Stator/rotor teeth width	$w_{ts/r}$	Depends on B_{gp} and $B_{ts/r}$	Peak rotor bar current	I_{bar}	Depends on A_{sr} and J_r
Stator/rotor yoke width	$w_{ys/r}$	Depends on B_{gp} and $B_{ys/r}$	Actual torque	T	Depends on B_{gp} and I_{bar}

2.2. Equivalent circuit tool

Once the geometry is fully defined, the parameters of the equivalent circuit are computed based on the motor geometry and its material properties, Boglietti et al. (2011). The model is a T-equivalent circuit, see Fig. 3, considering the skin and proximity effects in both the stator and the rotor. In the stator windings, those effects are calculated as follow, Pyrhönen et al. (2008),

$$\frac{R_{ac}}{R_{dc}} = \varphi(\xi) + \frac{z^2-1}{3}\psi(\xi) \tag{5}$$

with the two functions $\varphi(\xi)$ and $\psi(\xi)$ being

$$\varphi(\xi) = \xi\frac{sinh(2\xi)+sin(2\xi)}{cosh(2\xi)-cos(2\xi)} \text{ and } \psi(\xi) = 2\xi\frac{sinh(\xi)-sin(\xi)}{cosh(\xi)+cos(\xi)}, \text{ with } \xi = h_c\sqrt{\frac{1}{2}\frac{\omega\mu_0}{\rho_{Cu}}\frac{w_c}{w_{ss}}} \tag{6), (7) and (8)}$$

the reduced conductor height ξ, and z, ω, μ_0, w_c, h_c, w_{ss}, ρ_{Cu} denoting the number of conductor layers in a slot, the angular electrical frequency, the permeability of vacuum, the conductor width, the conductor height, the width of the stator slot and the conductivity of copper, respectively. A recursive algorithm is used to compute the skin and proximity effects on the rotor resistance, Boglietti et al. (2011), Pyrhönen et al. (2008) and Boldea and Nasar (2010). The iron losses are computed using Bertotti's model which is based on the Steinmetz equation and the loss separation model introduced by Jordan, Krings and Soulard (2010). Bertotti's equation is described as

$$P_{fe} = k\left(k_H B^{\beta_H} f + k_C B^2 f^2 + k_E B^{1.5} f^{1.5}\right)\rho_{fe} V_{fe} \tag{9}$$

with k representing the additional losses due to the punching process, k_H, β_H, k_C, k_E, denoting the hysteresis, the eddy current and the excess Steinmetz coefficients and B, f, ρ_{fe}, V_{fe} standing for the magnetic flux density in iron, the electrical frequency, the mass density of iron as well as the volume of iron, respectively.

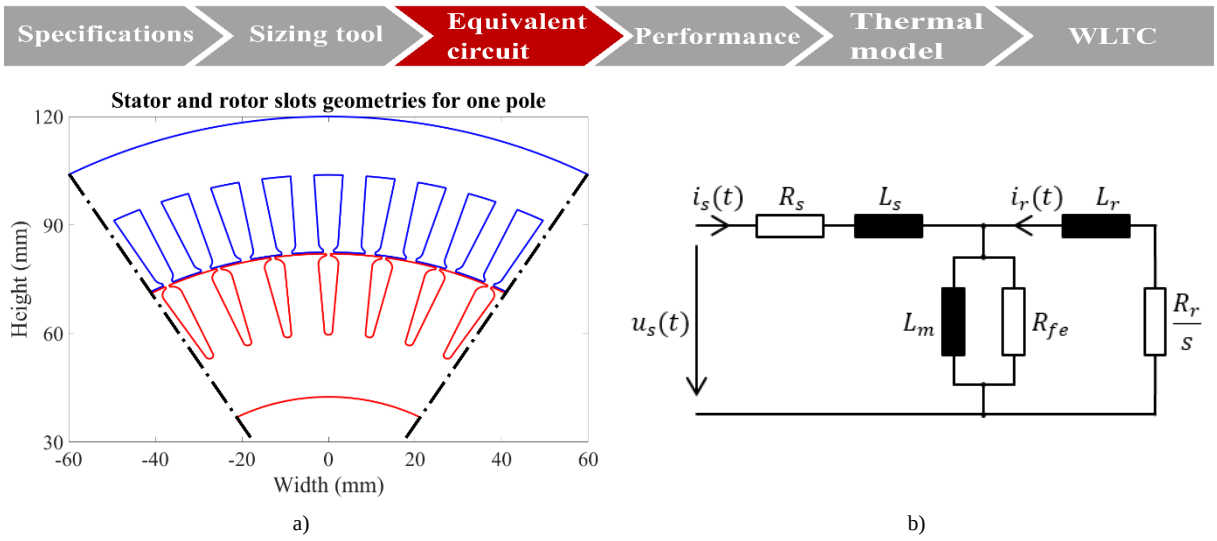

a) b)

Fig. 3 The geometry of the motor a) is used to compute the equivalent circuit parameters b).

Once the parameters of the T-equivalent circuit have been calculated, the model can be used to conduct a no-load and a locked rotor analysis. To get a better insight into the basic motor behavior, an open-loop voltage frequency control, with no current limit, is applied to drive the machine. The resulting torque versus speed characteristics of the reference traction drivetrain motor are displayed in Fig. 4. The peak torque requirement represents the maximum torque the motor and the inverter should be able produce for up to 30 s before a thermal derating is allowed. The continuous torque requirement depicts the desired torque in thermal equilibrium. It can be observed that at high speed the torque reserve is low, so the motor is not oversized. In base speed, that is below the nominal speed, the limiting factor is the current that can be provided by the inverter. When the motor is driven using a control algorithm which has a current limit implemented, like the control algorithm presented in section 2.3, the maximal torque reached is just above the peak operation requirement. Above the nominal speed, the

limiting factor is the voltage, as the induced voltage is proportional to the derivative of the flux and so it increases with the speed as shown in

$$V_{induced} = -\frac{d\phi(t)}{dt} = \omega \, sin(\omega t) \, \hat{\phi} \tag{10}$$

where $V_{induced}$, ϕ, ω, t denote the induced voltage, the magnetic flux, the angular electrical frequency and the time, respectively.

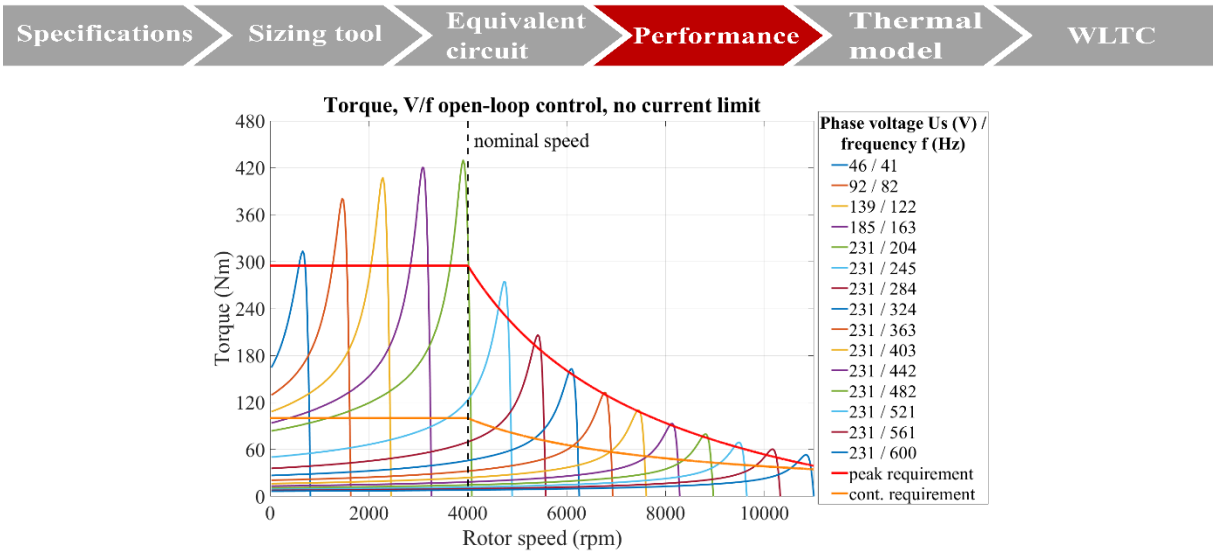

Fig. 4 Capability plot of the motor showing torque versus speed curves at different phase voltages U_s and electrical frequencies f.

2.3. Control strategy tool

There are many different torque control strategies for multi-phase induction motors, Parthan et al. (2017). Selecting the right one is a trade-off between different criteria such as response time, computational effort, company control strategy, etc. In BEVs, an important benchmark is the overall powertrain efficiency as it has a direct impact on the vehicle driving range, the battery volume and the total cost of ownership of the vehicle, Wu et al. (2015).

To further improve the topology optimization, the control strategy used in the vehicle must be considered during the motor design. Therefore, the Field Oriented Control (FOC) with variable flux is implemented in this tool, as described in Quang and Dittrich (2015). To select the optimal flux, the Maximum Torque Per Ampere (MTPA) algorithm considering iron losses is implemented, as presented in Hrkel et al. (2012). The rotor speed n is set to the target speed n^* and the actual torque T is set to the reference torque T^*. Then, the direct and the quadrature currents I_d and I_q are selected to minimize the stator phase current I_s while respecting the phase current and the phase voltage limits $I_{s,max}$ and $U_{s,max}$. This is described as

$$n = n^*, T = T^*, min|I_s|, \text{ with } |I_s| \leq I_{s,max} \text{ and } |U_s| \leq U_{s,max}. \tag{11}$$

As the voltage limit is already implemented in this MTPA method, the control algorithm can be applied to the whole operating range. Adopting this algorithm, the peak and continuous performance of the motor are computed as well as an efficiency map. In Fig. 5 a), the torque and power versus speed characteristics of the reference traction drivetrain motor are displayed. The peak operation phase current limit is 450 A_{rms}, the current limit in continuous operation is 160 A_{rms} and the DC-link voltage is 400 V. In Table 5, additional data concerning this motor are given. In Fig. 5 b), the analytically computed efficiency map of the motor is drawn. For the efficiency estimation, the copper and iron losses are considered but friction losses and additional losses due to harmonics are neglected.

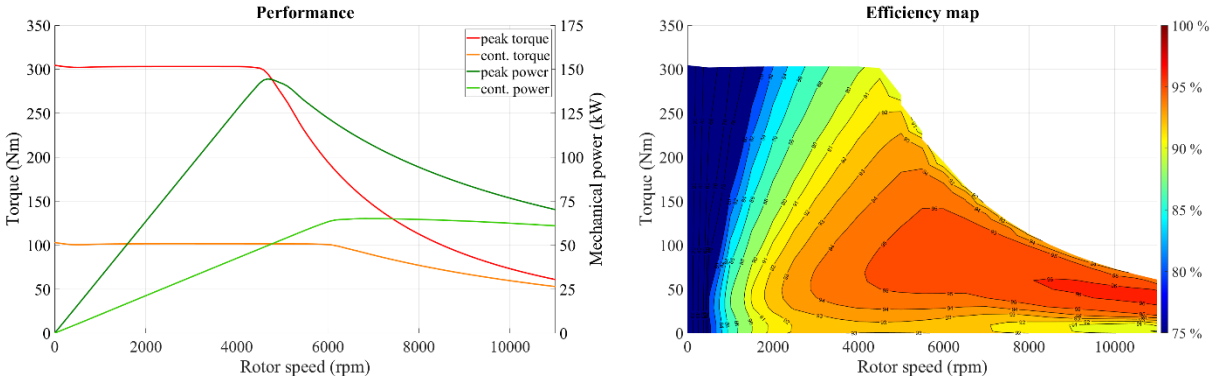

a) b)

Fig. 5 Performance of the motor, a) torque and power versus speed characteristics at peak and continuous operation and b) efficiency map.

2.4. Thermal tool

A lumped parameter thermal model, shown in Fig. 6, is generated based on the motor geometry and its materials properties, as derived in Boglietti et al. (2003). This simplified thermal model consists of thermal resistances representing the conductive and convection heat transfer of the different motor parts and current sources illustrating the heat flux into the machine. The system is assumed to be liquid-cooled, as is generally the case in automotive applications.

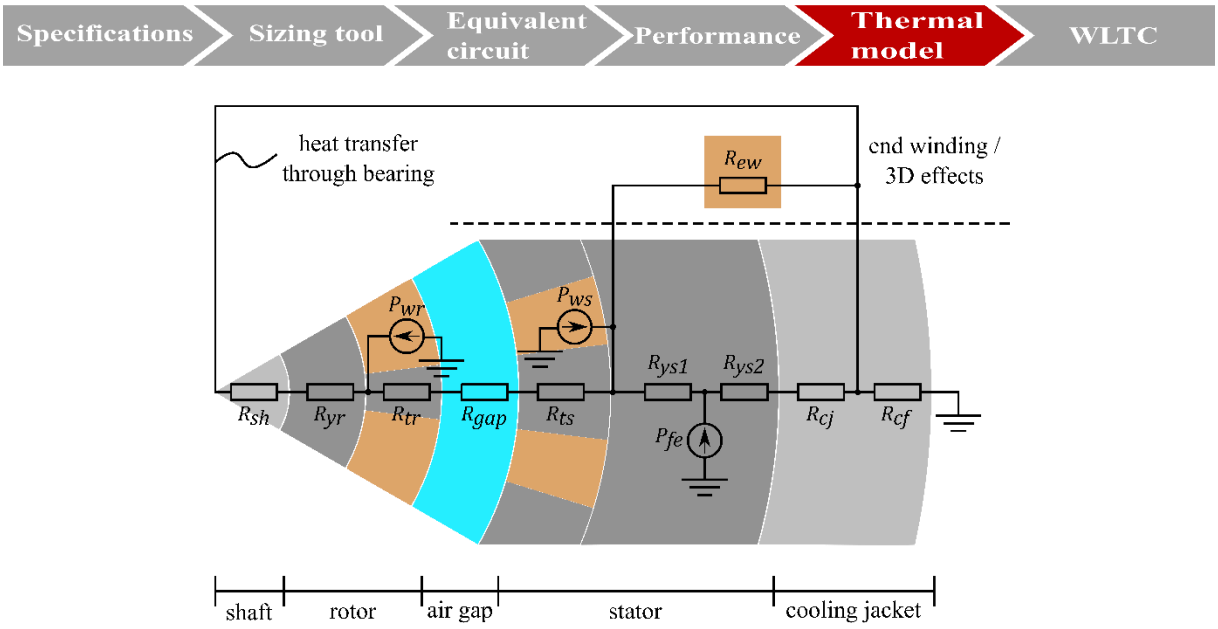

Fig. 6 Schematic view of the Lumped Parameter Thermal Model (LPTM) used to calculate the temperature in the motor (for illustrations, geometric dimensions are not to scale).

The heat flux is generated by the stator and rotor copper losses as well as the stator iron losses. These losses are computed in the performance block with the control described in section 2.3. Both the steady-state temperature distribution in the motor and the transient temperature behavior of the windings can be analyzed with LAMA. Subsequently, the equivalent circuit parameters are recalculated at the temperatures computed by the thermal model and the performance of the motor are also recomputed, in an iterative loop.

2.5. WLTC computation tool

Once the efficiency map is calculated, the WLTC computation tool is used to calculate the WLTC efficiency and energy consumption of a given vehicle. This allows for a simple and quick comparison of different motors as well as a comparison of the driving range estimated for the given car model. The tool considers vehicle parameters such as mass, frontal area, drag coefficient, as well as the efficiency of the gearbox and the power electronics (or inverter). The input parameters for the WLTC computation tool are summarized in Table 4. The WLTC speed over time data for class 3 (high power to weight ratio, > 34 W/kg) vehicles is plotted in Fig. 7 next to the torque versus speed points of the reference traction system. A VW e-Golf with a BRUSA drive system is used as an example. This tool translates abstracts powertrain and vehicle specifications into a comprehensible and commonly used benchmark, the driving range.

Table 4. Input parameters for the WLTC computation tool.

Description	Variable	Type	Description	Variable	Type
Motor efficiency map	η_{motor}	Motor	Car mass	$m_{vehicle}$	Vehicle
Motor mass	m_{motor}	Motor	Car frontal area	A_{front}	Vehicle
Motor inertia	I_{motor}	Motor	Roll coefficient	c_{roll}	Vehicle
Gearbox efficiency map	$\eta_{gearbox}$	Gearbox	Drag coefficient	c_{drag}	Vehicle
Gearbox ratio	$r_{gearbox}$	Gearbox	Wheel inertia	I_{wheel}	Vehicle
Power electronics efficiency map	η_{PE}	Power electronics	Wheel diameter	d_{wheel}	Vehicle
Cycle data (speed over time)	(v, t)	WLTC	Wheel bearing efficiency	η_{wheel}	Vehicle
Air density	ρ_{air}	Environment			

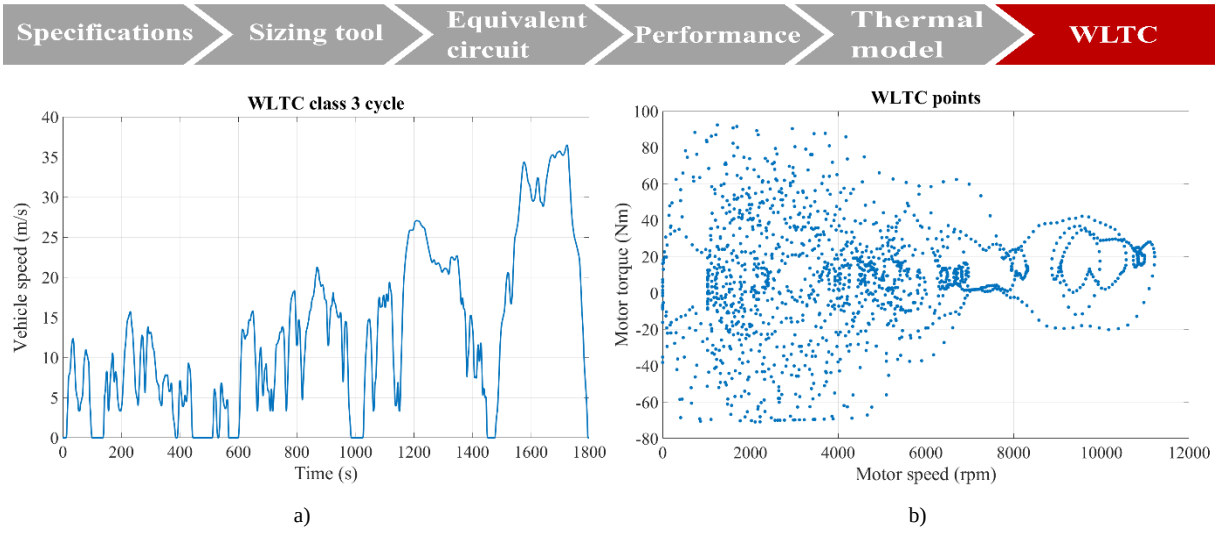

a) b)

Fig. 7 WLTC class 3 speed over time data a), torque versus speed points of a drive system performing the WLTC in a VW e-Golf b).

2.6. Cost computation tool

The cost is a key performance indicator and is therefore considered during the design optimization process. The monetary cost of the motor active parts is estimated using their mass and the market price of iron laminations, copper and possibly aluminum. A supplement is considered for the rest of the components and the manufacturing process.

3. Comparison of LAMA results with measurements

A *BRUSA* 6-pole motor with the specifications given in Table 5 is used to assert the validity of the analytical model implemented in LAMA. The measurements are carried out according to the international standard IEC 60034-28, (2012).

Table 5. Properties of the traction drivetrain induction motor used as reference in this paper.

Description	Variable	Value	Unit	Description	Variable	Value	Unit
Active length	l_a	123	mm	Number of phases	m	3	-
Stator outer diameter	d_{os}	240	mm	Number of pole pairs	N_{pp}	3	-
Rotor outer diameter	d_{is}	164	mm	Nominal/maximal speed	n_N	4000 / 11000	rpm

A no-load analysis is performed for different frequencies. In Fig. 8 and Fig. 9, the results of the test performed at nominal speed are presented for both measurements and analytical computations. For this motor, the nominal speed is 4000 rpm which leads to an electrical frequency of 200 Hz. In no-load conditions, LAMA estimates the current accurately for a given operating point (voltage and frequency). The relative difference is less than 10 % on the entire range displayed in Fig. 8 a). As can be observed in Fig. 8 b), the iron losses are underestimated at higher voltages. The maximal relative error is 25 % at 145 V_{rms}. A deviation is expected, especially at high voltages, as the Steinmetz equation used to compute the iron losses is a fundamental model neglecting any harmonic content which increases with the saturation. Furthermore, the Steinmetz equation relies on roughly estimated material properties and its accuracy should therefore be considered with caution.

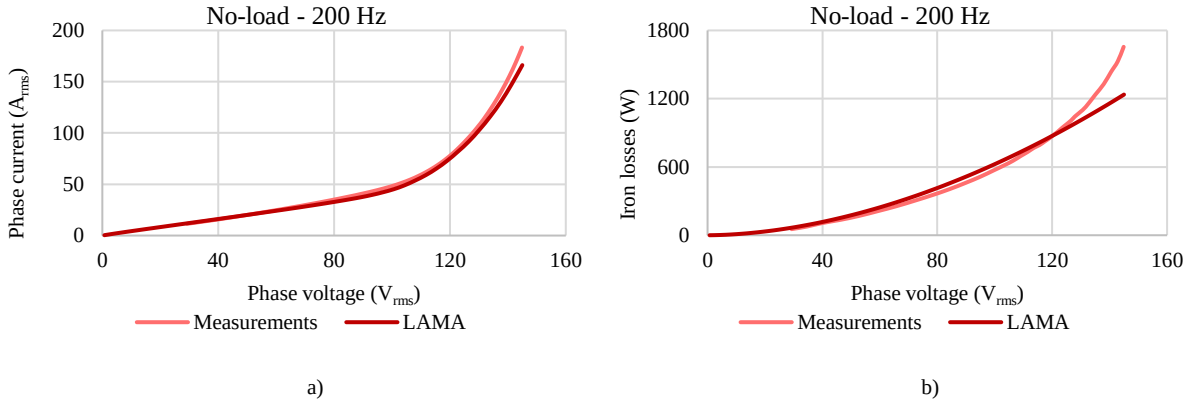

Fig. 8 No-load results at 200 Hz, a) phase current versus phase voltage, b) iron losses vs voltage.

In Fig. 9, the magnetizing inductance is displayed. Despite a deviation in saturation estimation, the relative divergence is below 10 %. The magnetizing inductance is not measured but derived from measured values following the procedure described in the international standard IEC 60034-28, (2012).

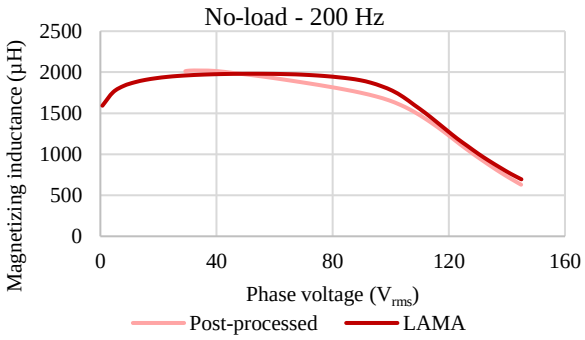

Fig. 9 Magnetizing inductance versus phase voltage characteristics in no-load operation, at nominal speed.

The saturation in the traction motor is more pronounced during the no-load test compared to the locked rotor test. Therefore, the verification of the saturation computation is done with the no-load measurements. For the sake of brevity, the results of the locked rotor analysis are not presented in this paper. To assert the performance of the motor, load tests are performed at different frequencies and voltages. The load test presented in Fig. 10 is effectuated at an electrical frequency of 200 Hz and a phase voltage of 120 V_{rms}. For the torque versus phase current characteristics shown in Fig. 10 a), a relative difference of around 9 % can be observed between measurements and computed data. The relative deviation comparing the torque versus speed characteristics in Fig. 10 b) lies around 11 %. In load operation, LAMA slightly overestimates the performance of the motor. Note that mechanical losses, i.e. drag, friction and bearing losses, are present in the measurements but not integrated in the analytical tool. This partially explains the disparity between measurements and computational results.

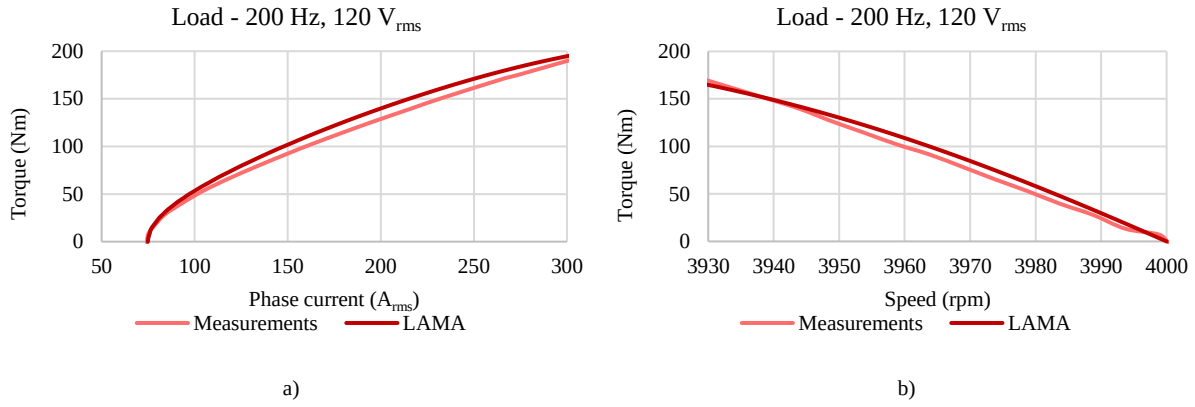

Fig. 10 Load analysis at an electrical frequency of 200 Hz and a phase voltage of 120 V_{rms}, a) torque versus phase current characteristics, b) torque versus rotational speed curve.

Fig. 11 shows the torque versus speed characteristics of the traction drivetrain motor in peak operation, namely a phase current limit of 450 A_{rms} is enforced and the DC-link voltage is 400 V. The control algorithm implemented in LAMA is used to drive the motor at peak operation. Once again, LAMA slightly overestimates the performance of the motor. At nominal speed (4000 rpm) the relative torque deviation is 2 %, at twice the nominal speed (8000 rpm) the relative deviation is 4 % and at maximal speed (11000 rpm) the relative deviation is 20 %. Again, the divergence increases with speed, partly due to the rising prevalence of the mechanical losses. Furthermore, the divergence in iron loss estimation increases with the speed which also leads to a higher deviation in performance estimation.

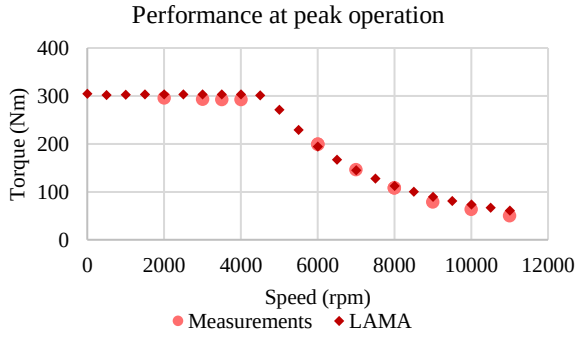

Fig. 11 Comparison between LAMA and measurements of the torque over speed during peak performance operation with a phase current limit of 450 A_{rms} and a DC-link voltage of 400 V.

4. Conclusion

This paper shows that the performance of an induction motor can be accurately evaluated considering the machine non-linearities and the control strategy using analytical models complemented by empirical factors. With these analytical models, a very fast computation time is achieved. Therefore, a large design space can be

covered, and a global sensitivity analysis or an optimization can be conducted in a short time. The calculation time per motor is approximately 200 times faster using LAMA compared to FEM tools. Furthermore, section 3 demonstrates that speed does not come at the cost of precision. The accuracy of the no-load analysis is acceptable even if the iron losses estimation could be improved at high saturation. At peak operation, precise results are obtained. A relative deviation below 5 % is achieved for speeds up to twice the nominal speed. To further improve the accuracy of the performance and efficiency estimation, an analytical tool to compute the mechanical losses is currently being developed.

For the sake of brevity, only induction motor design is shown in this paper. However, the development of a tool to design buried permanent magnet synchronous machines is ongoing at *BRUSA* since synchronous motors are widely used for traction drivetrain applications due to their high power density.

References

Boglietti, A., Cavagnino, A., & Lazzari, M. (2011). Computational Algorithms for Induction Motor Equivalent Circuit Parameter Determination-Part I: Resistances and Leakage Reactances. *IEEE Trans. Ind. Electron.*, 3723-3733.

Boglietti, A., Cavagnino, A., & Lazzari, M. (2011). Computational Algorithms for Induction Motor Equivalent Circuit Parameter Determination-Part II: Skin Effect and Magnetizing Characteristics. *IEEE Trans. Ind. Electron.*, 3734-3740.

Boglietti, A., Cavagnino, A., Lazzari, M., & Pastorelli, M. (2003). A Simplified Thermal Model for Variable-Speed Self-Cooled Industrial Induction Motor. *IEEE Trans. Ind. Electron.*, 945-952.

Boglietti, A., Cavagnino, A., Lazzari, M., & Vaschetto, S. (2012). Preliminary induction motor electromagnetic sizing based on a geometrical approach. *IET Electric Power Applications*, 583-592.

Boldea, I., & Nasar, S. A. (2010). *The Induction Machines Design Handbook* (Second ed.). CRC Press, Taylor & Francis Group.

Hrkel, M., Vittek, J., & Biel, Z. (2012). Maximum torque per ampere control strategy of induction motor with iron losses. *2012 ELEKTRO*, 185-190.

IEC 60034-28. (2012). Rotating Electrical Machines – Part 28: Test methods for determining quantities of equivalent circuit diagrams for three-phase low-voltage cage induction motors. Geneva, Switzerland.

J.P.Morgan. (2018, October 10). *electric-vehicles*. Retrieved from J.P. Morgan: https://www.jpmorgan.com/global/research/electric-vehicles

Krings, A., & Soulard, J. (2010). Overview and Comparison of Iron Loss Models for Electrical Machines. *Journal of Electrical Engineering*, 162-169.

McKinsey. (2018, May). *the global electric vehicle market is amped up and on the rise*. Retrieved from McKinsey & Company: https://www.mckinsey.com/industries/automotive-and-assembly/our-insights/the-global-electric-vehicle-market-is-amped-up-and-on-the-rise

Parthan, A., Suresh, L. P., & Raj, J. R. (2017). A brief review on torque control of induction motor. *2017 International Conference on Circuit, Power and Computing Technologies (ICCPCT).* Kollam, India: IEEE.

Pyrhönen, J., Jokinen, T., & Hrabovcová, V. (2008). *Design of Rotating Electrical Machines.* John Wiley & Sons, Ltd.

Quang, N. P., & Dittrich, J.-A. (2015). *Vector Control of Three-Phase AC Machines.* Berlin: Springer.

Raconteur. (2018). *infographics - electrifying-autos.* Retrieved from Raconteur: https://www.raconteur.net/infographics/electrifying-autos

Wu, G., Inderbitzin, A., & Bening, C. (2015). Total cost of ownership of electric vehicles compared to conventional vehicles: A probabilistic analysis and projection across market segments. *Energy Policy*, 196-214.